SECTION VII   TRAVELING WAVES AND THERMAL CONVECTION

TRAVELING WAVES IN AXISYMMETRIC CONVECTION: THE ROLE OF SIDEWALL CONDUCTIVITY

Dwight BARKLEY and Laurette S. TUCKERMAN
Department of Physics and Center for Nonlinear Dynamics, University of Texas, Austin, TX 78712, USA

The results of a full numerical simulation of Rayleigh–Bénard convection in a cylindrical container of aspect ratio five are reported. Near onset, convection takes the form of five concentric rolls, which in fluids of moderate to large Prandtl number, are stable to nonaxisymmetric perturbations. As the Rayleigh number is increased, these rolls are succeeded by traveling waves when the sidewalls of the container have high thermal conductivity. For insulating sidewalls, transition occurs instead to steady four-roll states. A complete two-parameter phase diagram connecting these two scenarios is presented.

1. Introduction

In a recent paper [1] we described the occurrence of traveling waves in simulations of Rayleigh–Bénard convection in a cylindrical container. While many studies, both experimental [2, 3] and theoretical [4–8], have explored time-dependent patterns in convection, our study was unique in that we considered the role of thermally conducting sidewalls in the formation of traveling waves. Our main observation was that in cylinders whose sidewalls are good thermal conductors, traveling waves occur for simple (non-binary) fluids. We found that for moderate to high Prandtl number fluids, the axisymmetric states (both steady and oscillatory) near convective onset are not subject to the nonaxisymmetric instabilities [9] and chaotic dynamics [2] observed near convective onset in lower Prandtl number fluids. Thus, the combination of high Prandtl number and high sidewall conductivity is, in many cases, sufficient to produce axisymmetric traveling waves near the onset of convection.

Our purpose here is to expand on this earlier work. Previously we described only the cases of perfectly insulating and perfectly conducting lateral sidewalls. Here we describe the convective dynamics near onset over the entire range of sidewall conductivities. Our approach is the same as before: we use numerical techniques (both time-stepping and steady-state continuation) to solve the full time-dependent Boussinesq equations for a cylindrical geometry. We then use dynamical systems theory to analyze the bifurcations between various steady and oscillatory states.

2. Description of system and numerical methods

Our results have been obtained from an initial-value pseudospectral code [10]. We have developed methods which adapt the same code to perform steady state continuation [11] and linear stability analysis [12]. All computations reported are for an aspect ratio (radius/depth) $\Gamma = 5$. We have used 50 Chebyshev polynomials in the radial direction r and 16 in the vertical direction z, and have checked numerical accuracy by doubling this spatial resolution. The timestep used is 0.002, the maximum allowed by the Courant condition. (All times are expressed in units of the vertical thermal diffusion time $t_v = d^2/\kappa$, where d and κ are the depth and thermal diffusivity of the fluid layer; distances are expressed in units of d.)

The plates at the top and bottom of the container, as well as the sidewalls, are rigid: boundary conditions $u_r = u_z = 0$ are imposed on the velocity. The top and bottom plates are taken to be perfect thermal conductors. To investigate the effect of lateral sidewalls with finite thickness and thermal conductivity, we imposed the hybrid boundary condition [13] $\mu h + \partial_r h = 0$ on the sidewalls, where h is the temperature deviation from the conductive profile. For $\mu \equiv \pi \kappa_w \tanh(\pi d_w)$ this hybrid boundary condition approximates sidewalls with a finite thermal diffusivity κ_w and thickness d_w. We shall generally refer to μ simply as the sidewall conductivity.

The system, i.e. the equations and boundary conditions, is invariant under the operation of z-reflection, defined by

$$(u_r, u_\theta, u_z, h)(r, \theta, z)$$

$$\rightarrow (u_r, u_\theta, -u_z, -h)(r, \theta, -z).$$

This symmetry will prove to be important in the dynamics we now describe.

3. Results

All detailed results reported here are for an aspect ratio $\Gamma = 5$ and a Prandtl number $Pr = 10$. For these parameter values we have found that, near the onset of convection, axisymmetric patterns are stable, once obtained, to nonaxisymmetric perturbations of the form $\exp(im\theta)$ for all $m \leq 5$. We shall first describe the scenario obtained as a function of Rayleigh number for perfectly conducting sidewalls. This scenario illustrates both the nature of the traveling waves which we have investigated and the global bifurcation which triggers them. We then briefly discuss the case of perfectly insulating sidewalls. Finally, we connect these two limiting cases in a comprehensive picture showing the dynamics of the system as a function of both Rayleigh number and sidewall conductivity.

3.1. Conducting sidewalls

A schematic bifurcation diagram summarizing our findings for the case of perfectly conducting sidewalls ($\mu = \infty$) is shown in fig. 1. We use as the bifurcation parameter the reduced Rayleigh number $\varepsilon \equiv (Ra - Ra_c)/Ra_c$, where Ra is the Rayleigh number and Ra_c is the critical Rayleigh number for onset of convection. For $\Gamma = 5$, $Ra_c = 1734$.

We begin with a description of the stable states. For negative ε the conductive state is stable, as illustrated in phase portrait (c). At $\varepsilon = 0$, a supercritical bifurcation breaks the reflection symmetry, giving rise to two symmetrically-related stable five-roll states [phase portrait (d)]. Fig. 1(a) shows
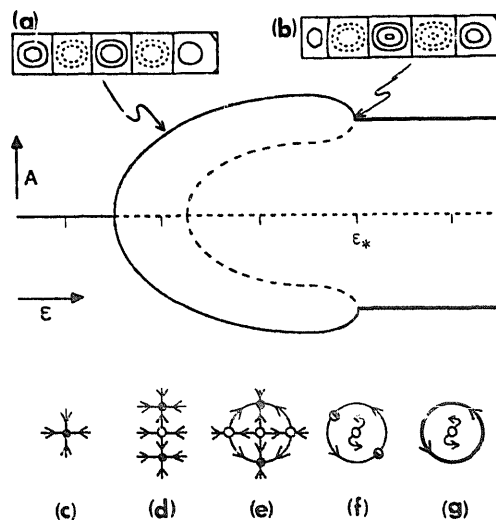

Fig. 1. Schematic bifurcation diagram for the case of conducting sidewalls. ε is the reduced Rayleigh number, and A is a coordinate which distinguishes between different states. (a) and (b) are numerically calculated streamfunction contours of representative five-roll steady states at two values of ε. Below the diagram are phase portraits at the five values of ε denoted by tick marks. Stable (unstable) states are denoted by solid (dashed) lines in the bifurcation diagram, and by solid (hollow) circles in the phase portraits. The traveling wave state (see fig. 2) is denoted by bold lines. In phase portrait (c), the conductive state is stable. In (d), a supercritical bifurcation from the conductive state has given rise to a pair of symmetrically related five-roll states. In (e) a second pair of (unstable) states has arisen via another supercritical bifurcation. The stable and unstable states approach one another and disappear via the saddle–node bifurcation in (f). This results in a heteroclinic orbit which becomes the limit cycle in (g).
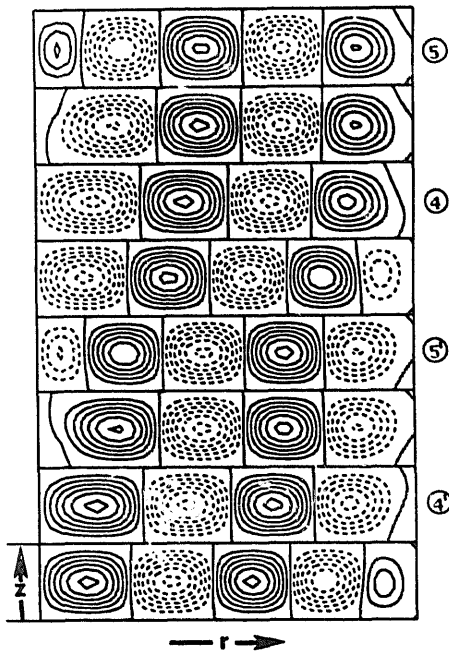
Fig. 2. Instantaneous streamfunction contours in the r–z plane of the traveling wave state at $\varepsilon = 1.39$. Solid (dashed) contours denote clockwise (counter-clockwise) flow. Contours are shown at times $t = 0$, 19, 27, 34, 70, 89, 97, and 104. The numbers label slowly varying quasi-five-roll and quasi-four-roll states.

Fig. 3. Nusselt number time series at the bottom plate for two values of ε. The lower time series is for $\varepsilon = 1.39$ (the same value as in fig. 2), and shows approximately one oscillation period just above the onset of traveling waves. The upper is for $\varepsilon = 2.60$. The period diverges at onset while the amplitude of oscillation remains approximately constant.

numerically obtained streamfunction contours in the r–z plane for one of these two symmetrically-related states. The left edge of the plot is at $r = 0$, i.e. the center of the cylinder; the right edge of the plot is at the cylinder's sidewall. Solid and dashed contours denote clockwise and counterclockwise flow, respectively. The five-roll state corresponding to the lower branch of the pitchfork is obtained from that corresponding to the upper branch by z-reflection, or equivalently, by changing the solid contours of fig. 1(a) to dashed contours (and vice versa) and reflecting the contours in z. In phase portraits (c)–(g), as well as throughout this paper, z-reflection corresponds to reflection through the origin.

As ε is increased, the size of the central (leftmost) roll decreases [compare figs. 1(a) and (b)], until it disappears at a critical value $\varepsilon_* = 1.3843$, when the stable five-roll state gives way to a large-amplitude low-frequency traveling wave (limit cycle), indicated by bold lines in fig. 1.
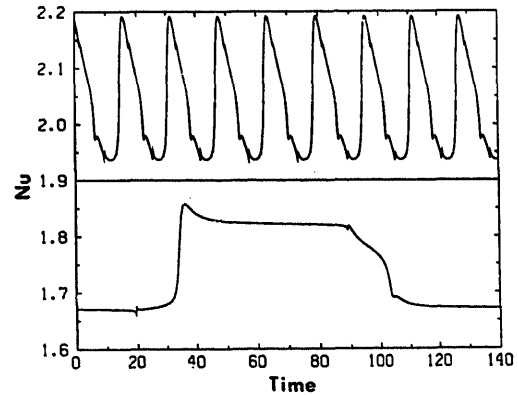
Shown in fig. 2 are instantaneous streamfunction contours for the traveling wave state just above its onset ($\varepsilon = 1.39$). The central roll becomes smaller and is then annihilated, while new rolls are continually created at the sidewall, leading to an alternation between four and five rolls (for reasons which shall become clear). The eight contour plots in fig. 2 have been chosen to illustrate this, and are not equally spaced in time. The transition to periodic behavior is a *symmetry-restoring* bifurcation, as the states in the second half of the limit cycle are related by z-reflection to those of the first half; this symmetry is manifested in the limit cycle of phase portrait (g) (see fig. 1) as well.

In fig. 3 we show the Nusselt number for the bottom plate* as a function of time at two values of ε. The lower plot is just above the onset of traveling waves ($\varepsilon = 1.39$ as in fig. 2), and shows approximately one period of oscillation. The "glitches" at times 19 and 89 occur when the system loses a central roll [see fig. 2]. The rapid

*By Nusselt number of the bottom plate we mean the ratio of the total heat transferred through the bottom plate to the heat that would be transferred by conduction alone. Only in the case of perfectly insulating sidewalls are the Nusselt numbers of the top and bottom plates the same.

changes in Nusselt number (at times approximately 34 and 104) result from the gain of rolls at the sidewall. Note that just above onset, the traveling waves pause for considerable time in each of the two quasi-steady five-roll states.

The upper plot in fig. 3 is for ε well above the transition to traveling waves (ε = 2.60). The oscillation period is greatly reduced and the system now passes quickly through the five-roll states. While the average Nusselt number increases with ε, the amplitude of the oscillations does not. Thus the traveling waves are born with finite amplitude, and the period of the oscillations diverges at onset. Hence the traveling wave state does not arise from a Hopf bifurcation but rather from a global (heteroclinic) bifurcation.

Returning to fig. 1, we describe the scenario leading to the global bifurcation which triggers the traveling waves. After the first supercritical bifurcation [phase portrait (d)], the conductive branch undergoes a second supercritical bifurcation to a pair of *unstable* five-roll states [phase portrait (e)]. Because these new states are born from the already unstable conductive state, they inherit trajectories which terminate on the stable five-roll states. Thus the new states, like the conductive state, are unstable. As ε is increased beyond the second supercritical bifurcation, the stable and unstable five-roll states approach one another (pairwise) and collide in saddle–nodes [denoted by the half-filled circles in phase portrait (f)]; the connections between the steady states form the heteroclinic orbit. After the five-roll states disappear in the saddle–node bifurcations, trajectories no longer terminate on fixed points, but proceed around a limit cycle [phase portrait (g)].

We note that there are two scaling behaviors expected at such a heteroclinic bifurcation. First, because the onset of traveling waves occurs at a saddle–node bifurcation, the Nusselt number (or virtually any other measurable quantity) should approach its value at ε_* like $(\varepsilon_* - \varepsilon)^{1/2}$. Second, the period of the traveling waves is expected to diverge like $T \sim (\varepsilon - \varepsilon_*)^{-1/2}$. We have verified both of these behaviors in our simulations, though

the range in ε over which we find these scalings is quite small ($|\varepsilon - \varepsilon_*| < 10^{-3}$).

3.2. Insulating sidewalls

We now turn to the case of perfectly insulating sidewalls ($\mu = 0$), summarizing our findings in another schematic bifurcation diagram (fig. 4). Traveling waves are not observed. Upon increasing ε, the primary five-roll branch again loses stability via a saddle–node bifurcation, at a value $\varepsilon_* = 1.4119$ quite close to the transition point $\varepsilon_* = 1.3883$ for perfectly conducting sidewalls. However, this time the transition is to another *steady state*, one having four rolls. A streamfunction contour plot for one of two symmetrically-related stable four-roll states is shown in fig. 4(a). The transition is strongly hysteretic: each four-roll branch can be followed by decreasing ε until it disappears via a saddle–node bifurcation (of Eckhaus type [14]) at ε = 0.1035, inducing a transition back to the primary five-roll branch.

The phase portraits (b)–(e) illustrate how the four-roll states intercept trajectories in such a way
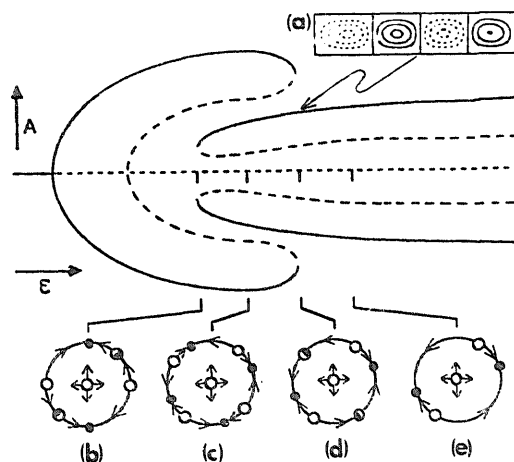

Fig. 4. Schematic bifurcation diagram for the case of insulating sidewalls. Conventions are the same as in fig. 1. The diagram differs from fig. 1 by the absence of traveling waves and by the presence of additional steady four-roll states (a). Phase portrait (b) shows the emergence of two pairs of four-roll states via saddle–node bifurcation, leading to the bistable situation with eight convective steady states shown in (c). (d) depicts the saddle–node bifurcation causing the disappearance of the five-roll states, leaving only the four-roll states (e).

as to prevent the formation of the limit cycle. Phase portrait (b) shows the emergence of the four-roll states in a pair of saddle–node bifurcations (denoted by half-filled circles); the stable and unstable five-roll states are marked with solid and hollow circles as before [see fig. 1(e)]. Phase portrait (c) shows the coexistence of the four-roll and five-roll states (the four-roll states are at the upper right and lower left; the five-roll states are at the upper left and lower right). Eventually the five-roll states collide in the pair of saddle–node bifurcations shown in (d). Thereafter, only the four-roll states exist on the invariant circle which forms the limit cycle (traveling waves) in the case of conducting sidewalls [compare figs. 4(d) and (e) with figs. 1(f) and (g)].

3.3. Two-parameter phase diagram

We now turn to our principal result and show how the above two scenarios are connected. Our findings are summarized in the phase diagram (bifurcation set) shown in fig. 5, illustrating the behavior of the system as a function of the reduced Rayleigh number ε and sidewall conductivity μ. Loci of saddle–node bifurcations delimit four regions, the dynamics in each of which is depicted by a schematic phase portrait. The curves 4a and 4b are the numerically computed saddle–node bifurcations at the low-ε and high-ε ends of the four-roll branch; curve 5b marks the saddle–node bifurcation terminating the five-roll branch. Bifurcation diagrams at four values of μ are also provided. Fig. 6 shows phase portraits for each of the four regions of fig. 5 obtained directly from our numerical simulations.

The behavior at low sidewall conductivity is just that described for the case of perfectly insulating sidewalls ($\mu = 0$), and the lower bifurcation diagram (δ) is the same as fig. 4. For larger values of μ [bifurcation diagram (γ)], the four-roll branch terminates in a second saddle–node bifurcation at

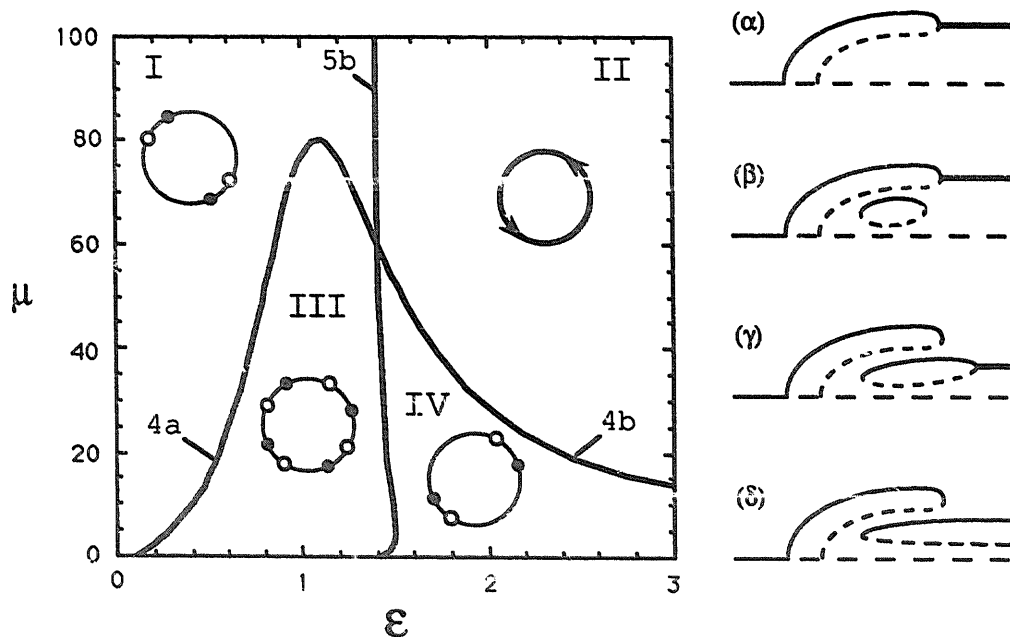

Fig. 5. Phase diagram showing the behavior of the system as a function of the two parameters μ and ε. The curves 4a and 4b mark the numerically computed saddle–node bifurcations at the low-ε and high-ε ends of the four-roll branch; curve 5b marks the saddle–node bifurcation terminating the five-roll branch. These curves delimit four regions (I–IV) with different dynamics. Each region contains a schematic phase portrait similar to those of figs 1 and 4. In region I, only five-roll states exist. Region II is the traveling wave regime. In region III, four- and five-roll states coexist, with separate basins of attraction. Region IV contains only four-roll states. To the right are bifurcation diagrams (α–δ) for four different values of μ. The conventions for the diagrams are as those of figs. 1 and 4, but only the upper half of each is shown.
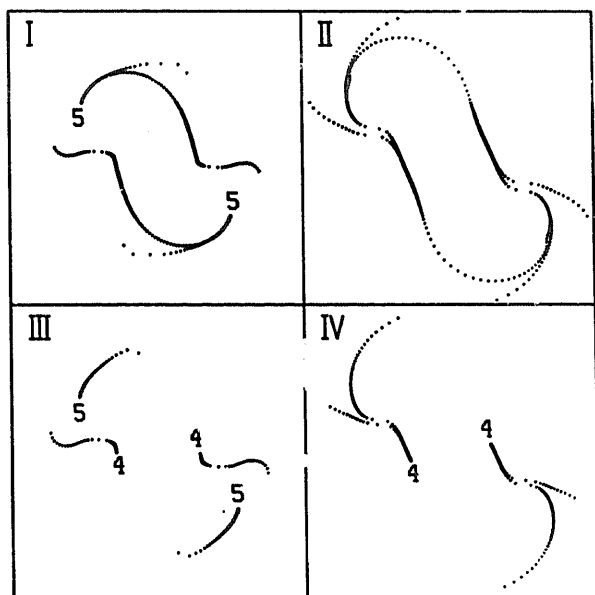
Fig. 6. Numerically computed phase portraits corresponding to the four regions I–IV of fig. 5. The parameter values are: (I) $\varepsilon = 1.0, \mu = 90$, (II) $\varepsilon = 2.0, \mu = 80$, (III) $\varepsilon = 1.1, \mu = 30$, (IV) $\varepsilon = 1.9, \mu = 15$. The coordinates are the projections onto the most unstable eigenvectors of the conductive state (at $\varepsilon = 1.40$). In each case four trajectories are shown whose initial conditions are approximately proportional to these eigenvectors. The numbers 4 and 5 are used to denote trajectories that terminate on stable four- and five-roll states. Points are equally spaced in time, indicating the speed of the trajectories through different areas of phase space.

high ε (curve 4b). Thus the four-roll branches are, in fact, isolas. The saddle–nodes at the upper end of the four-roll branches produce traveling waves by the same kind of global bifurcation which produces them in the highly conducting case. Now, however, near onset the traveling waves spend long periods of time in quasi-steady four-roll states.

The larger the value of μ, the narrower the range of ε over which the four-roll branch exists. Above $\mu = 60$, the curves 4b and 5b cross, so that high-ε termination of the four-roll branch occurs below that of the five-roll branch [bifurcation diagram (β)]. Thus, above $\mu = 60$, the curve of five-roll saddle–node bifurcations (5b) marks the transition to traveling waves, and below $\mu = 60$, this transition occurs along curve 4b. (In [1], this value of μ is mistakenly given as 33.) At $\mu = 80$, curves 4a and 4b meet, and the four-roll branch

disappears altogether: for higher μ, the situation is identical to that of perfectly conducting sidewalls [bifurcation diagram (α)].

The crossing of the curves 4b and 5b defines the global codimension-two bifurcation consisting of two pairs of saddle–nodes on the invariant circle. While no secondary bifurcations are to be expected in the vicinity of this point, it does provide the organizing center for the dynamics which we have discussed: the dynamics in each of the four regions arises from small perturbations of this degenerate situation.

(We note that even for perfectly insulating sidewalls, the four-roll branches terminate in saddle–node bifurcations at values of ε above those shown. Specifically, the curve 4b meets the ε-axis at $\varepsilon = 6.23$. However, at low values of μ, this curve does not mark the transition to traveling waves. Instead the system makes a transition to a steady *three-roll* state. For $\mu = 0$ we have followed the three-roll branches down to $\varepsilon = 2.30$, where they too terminate in saddle–node bifurcations. We have found it difficult to track the locus of three-roll saddle–node bifurcations for $\mu > 4$, but we do not believe that the three-roll branches exist for large values of μ; nor that they influence the limit cycles of region II.)

4. Discussion and conclusion

We now discuss the relevance of our results to experiments and to other theoretical studies. While we have described the situation in detail for a single choice of aspect ratio and Prandtl number, we believe these dynamics to be a very general feature of axisymmetric convection. We have run simulations for other parameter values and have found that thermally conducting sidewalls generally promote traveling waves.

In our previous article [1], we studied the Prandtl number dependence of these scenarios (still for $\Gamma = 5$), and found the transition to be largely insensitive to Pr for Pr ≥ 5. For lower Prandtl numbers, several factors destroy the picture we

have described here. First, the value ε_* for onset of waves depends strongly on Pr, reaching a minimum of $\varepsilon_*(\mathrm{Pr} = 1.7) = 0.909$, and diverging to very large ε at $\mathrm{Pr} = 0.7$. Also, the domain of existence of the four-roll states changes, so that, for example, at $\mathrm{Pr} = 0.98$, four rolls may be observed even with conducting sidewalls. More physically relevant is the fact that below $\mathrm{Pr} = 5$, we have found the axisymmetric states to be unstable to a nonaxisymmetric perturbation of the form $e^{im\theta}$, with $m = 1$. (At $\mathrm{Pr} = 10$, we have tested the stability of the steady states (for $\mu = 0$ and ∞, $\varepsilon = 1.3$ and 1.5) by determining that the most unstable nonaxisymmetric eigenvector has a negative growth rate, and that of the periodic states (for $\mu = \infty$, $\varepsilon = 1.5$) by observing the decay of nonaxisymmetric perturbations in full three-dimensional nonlinear simulations.)

We have also performed simulations with $\Gamma = 7.5$, and $\mathrm{Pr} = 6.1$ (the parameters used in [9]). We observe (at different ε) the same transitions as described here: saddle–node bifurcations leading to traveling waves for thermally conducting sidewalls, and to the loss of a roll for thermally insulating sidewalls (the sidewalls used in [9] were close to insulating, with $\mu \approx 1.5$). We note, however, that these states are also subject to nonaxisymmetric instabilities in the relevant parameter range.

Finally, we point out that traveling waves of the type we examined were first predicted to occur by Pomeau and Manneville [4] and have in fact been observed in simplified model equations of convection by Pomeau et al. [5] in an axisymmetric geometry, and by Cross et al. [8] near a focus singularity at a corner. Nevertheless, such traveling waves have never been observed experimentally. Our full simulations show that this results from sidewalls with low thermal conductivity. Experiments are generally conducted with $\mu = \mathcal{O}(1)$, a regime for which we have never obtained travel-

ing waves. By exploring the full range of sidewall conductivities, we have found that there exist large regions of parameter space (such as region II of fig. 5) for which these waves can be obtained experimentally.

Acknowledgements

References

[1] L.S. Tuckerman and D. Barkley, Phys. Rev. Lett. 61 (1988) 408.

[2] A. Pocheau, V. Croquette and P. Le Gal, Phys. Rev. Lett. 55 (1985) 1094.

[3] I. Rehberg, E. Bodenschatz, B. Winkler and F.H. Busse, Phys. Rev. Lett. 59 (1987) 282.

[4] Y. Pomeau and P. Manneville, J. Phys. (Paris) 42 (1981) 1067.

[5] Y. Pomeau, S. Zaleski and P. Manneville, ZAMP 36 (1985) 367.

[6] L. Kramer, E. Ben-Jacob, H. Brand and M.C. Cross, Phys. Rev. Lett. 49 (1982) 1891.

[7] L. Kramer and H. Riecke, Z. Phys. B 59 (1985) 245.

[8] M.C. Cross, G. Tesauro and H.S. Greenside, Physica D 23 (1986) 12.

[9] G. Ahlers, D.S. Cannell and V. Steinberg, Phys. Rev. Lett. 54 (1985) 1373.

[10] C. Canuto, M.Y. Hussaini, A. Quateroni and T.A. Zang, Spectral Methods in Fluid Dynamics (Springer, Berlin, 1987).

[11] L.S. Tuckerman, to appear in Proc. 11th Int. Conf. on Num. Meth. in Fluid Dynamics, D.L. Dwoyer, M.Y. Hussaini and R.G. Voigt, eds. (Springer, Berlin, 1989).

[12] P.S. Marcus and L.S. Tuckerman, J. Fluid Mech. 185 (1987) 1.

[13] M.C. Cross, P.G. Daniels, P.C. Hohenberg and E.D. Siggia, J. Fluid Mech. 127 (1983) 155.

[14] V. Eckhaus, Studies in Nonlinear Stability Theory (Springer, Berlin, 1965).